



The First Integral Field Unit Spectroscopic View of Shocked Cluster Galaxies

Andra Stroe^{1,5} , Maryam Hussaini^{1,2} , Bernd Husemann³, David Sobral⁴ , and Grant Tremblay¹ ¹Center for Astrophysics | Harvard & Smithsonian, 60 Garden St., Cambridge, MA 02138, USA; andra.stroe@cfa.harvard.edu²University of Texas at Austin, Department of Astronomy, 2515 Speedway, Stop C1400 Austin, Texas 78712-1205, USA³Max Planck Institut für Astronomie, Königstuhl 17, Heidelberg, Germany⁴Department of Physics, Lancaster University, Lancaster LA1 4YB, UK*Received 2020 October 7; revised 2020 November 16; accepted 2020 November 17; published 2020 December 17*

Abstract

Galaxy clusters grow by merging with other clusters, giving rise to Mpc-wide shock waves that travel at 1000–2500 km s⁻¹ through the intracluster medium. To study the effects of merger shocks on the properties of cluster galaxies, we present the first spatially resolved spectroscopic view of five H α -emitting galaxies located in the wake of shock fronts in the low redshift ($z \sim 0.2$), massive ($\sim 2 \times 10^{15} M_{\odot}$), post-core passage merging cluster, CIZA J2242.8+5301 (nicknamed the “Sausage”). Our Gemini/Gemini Multi-Object Spectrograph-North integral field unit (IFU) observations, designed to capture H α and [N II] emission, reveal the nebular gas distribution, kinematics, and metallicities in the galaxies over >16 kpc scales. While the galaxies show evidence for rotational support, the flux and velocity maps have complex features like tails and gas outflows aligned with the merger axis of the cluster. With gradients that are incompatible with inside-out disk growth, the metallicity maps are consistent with sustained star formation (SF) throughout and outside of the galactic disks. In combination with previous results, these pilot observations provide further evidence of a likely connection between cluster mergers and SF triggering in cluster galaxies, a potentially fundamental discovery revealing the interaction of galaxies with their environment.

Unified Astronomy Thesaurus concepts: [Emission line galaxies \(459\)](#); [Galaxy evolution \(594\)](#); [Galaxy clusters \(584\)](#); [Metallicity \(1031\)](#); [Star formation \(1569\)](#); [Shocks \(2086\)](#)

Supporting material: data behind figure

1. Introduction

The most extreme overdensities in the Universe evolve into the most massive ($\sim 10^{15} M_{\odot}$) gravitationally bound objects, galaxy clusters. Overdense environments heavily influence the evolution of galaxies: the densest parts of local, relaxed clusters are dominated by elliptical galaxies, devoid of ongoing star formation (SF) and the cold gas necessary for any future SF episode, while at lower densities the fraction of star-forming, gas-rich galaxies is larger than in the core (e.g., Dressler 1980; Solanes et al. 2001; Lewis et al. 2002; Tanaka et al. 2004; Mahajan et al. 2010).

The role that relaxed clusters play in galaxy evolution is well established in the literature, but the picture is less clear for clusters undergoing a significant growth phase. Local, massive galaxy clusters gain most of their mass through mergers with less massive clusters, rather than infall of matter (Muldrew et al. 2015). In a simplified merger scenario, two clusters fall toward each other with speeds of thousands of km s⁻¹ and merge over the course of 1–2 Gyr (e.g., Ricker & Sarazin 2001). As the two clusters pass through each other, significant energy is injected into the intracluster medium (ICM) in the form of large-scale bulk disturbances, fast-traveling shocks, and cluster-wide turbulence. In the context of hierarchical structure formation, merging clusters are located at active nodes in the cosmic web and thus surrounded by an extensive network of filaments and smaller subclusters.

Merging clusters represent 30%–50% of the galaxy cluster population at $z < 1$ (Mann & Ebeling 2012; Andrade-Santos et al. 2017; Rossetti et al. 2017) and are of particular interest to the

community as they present some surprising reversals of the typical environmental trends found in relaxed clusters. Studies contrasting statistical samples of relaxed and merging clusters found that merging galaxy clusters have a higher density of emission-line, star-forming, and blue galaxies, with higher specific SF rates (sSFR), stronger barred morphological features and large gas reservoirs, and a higher fraction of active galactic nuclei (AGNs; Miller & Owen 2003; Cortese et al. 2004; Hwang & Lee 2009; Hou et al. 2012; Jaffé et al. 2012, 2016; Sobral et al. 2015; Stroe et al. 2015a, 2015b, 2017; Cairns et al. 2019; Yoon et al. 2019; Yoon & Im 2020).

One of the most spectacular merging galaxy clusters is CIZA J2242.8+5301 ($z = 0.188$, see Figure 1), nicknamed the “Sausage.” The cluster hosts a unique overdensity of star-forming galaxies, over 25 times denser than the average cosmic volume at the cluster redshift and a SF rate (SFR) density >15 times above the level of typical star-forming galaxies at the “cosmic noon” ($z \sim 2$ –3), the peak of cosmic SF (Stroe et al. 2014b, 2015b). The cluster star-forming galaxies are massive, more metal-rich with lower electron densities compared to field galaxies, and show evidence for outflows, driven either by supernovae or AGN (Sobral et al. 2015; Stroe et al. 2015b). Moreover, the “Sausage” displays evidence for sustained SF over timescales of 500 Myr, as well as large neutral gas reservoirs to fuel future SF episodes (Stroe et al. 2015a).

To understand the evolution of SF in cluster galaxies, we must take into account the extraordinary merger history of the “Sausage” cluster. The “Sausage” cluster went through a massive merger <1 Gyr ago, along the north–south direction, in the plane of the sky, between two progenitors, each $\sim 10^{15} M_{\odot}$ with a relative speed of 2000–2500 km s⁻¹ (van Weeren et al. 2011; Stroe et al. 2014a; Jee et al. 2015). Two symmetric, fast-moving

⁵ Clay Fellow.

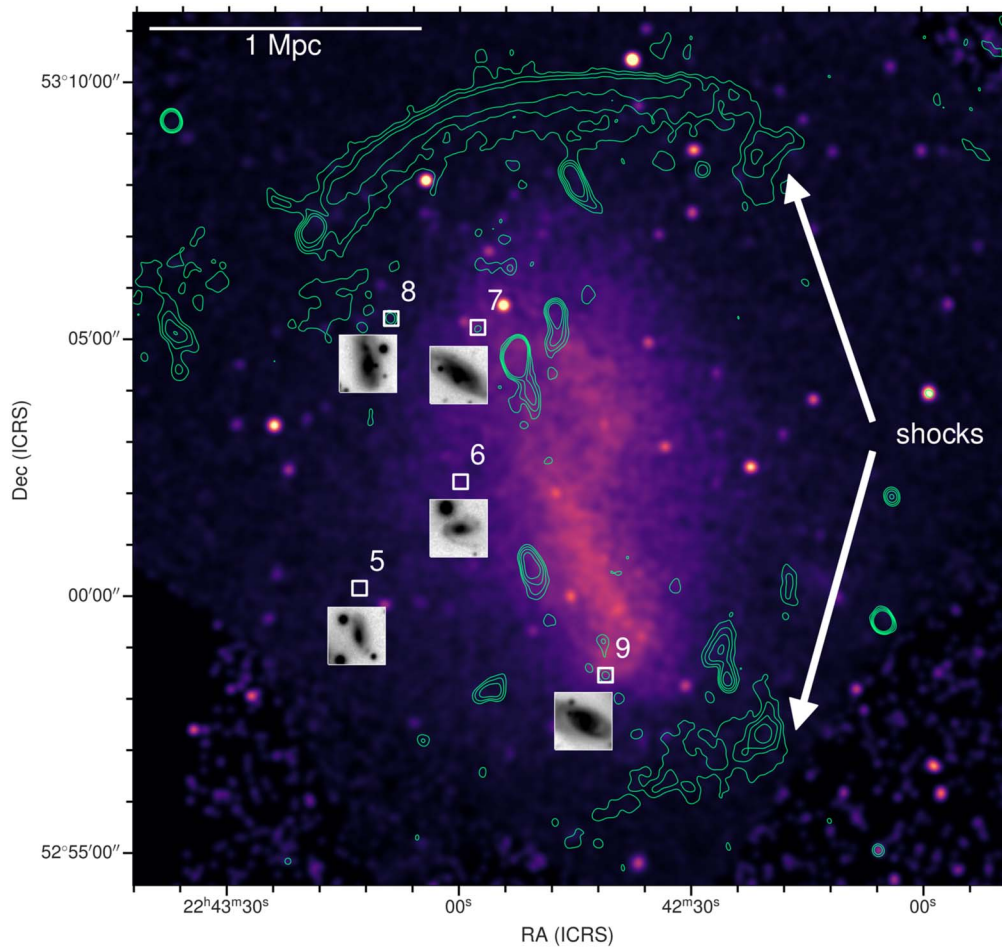


Figure 1. Our five shocked cluster galaxies in the “Sausage” cluster. Radio contours at 300 MHz from the Giant Metrewave Radio Telescope (Stroe et al. 2013) are drawn over a Chandra X-ray image (Ogrea et al. 2014). The cluster has undergone a major merger in the plane of the sky, as evidenced by the elongated X-ray distribution. The large-scale arc-like patches of radio emission located toward the north and south of the cluster trace large-scale shock waves induced by the merger 0.5–1 Gyr ago. The white squares mark the positions of the targets followed-up with Gemini Multi-Object Spectrograph (GMOS) integral field unit (IFU) spectroscopy. We display a $10'' \times 10''$ ($31.4 \text{ kpc} \times 31.4 \text{ kpc}$) *i*-band Subaru/Suprime-Cam (Jee et al. 2015) zoom-in image on each target.

($\sim 1000\text{--}2500 \text{ km s}^{-1}$) shocks were produced as the two subclusters passed through each other 0.5–1 Gyr ago. The shock waves propagated through the ICM along the merger axis and are revealed as arc-like, Mpc-wide patches of diffuse radio emission at the cluster outskirts (Figure 1, e.g., Stroe et al. 2013).

To explain the unusual nature of the star-forming galaxies in the “Sausage” cluster, Stroe et al. (2015b), in agreement with models from Roediger et al. (2014) and Ebeling & Kalita (2019), speculate that the traveling shocks pass through the gas-rich cluster galaxies, disrupt the gas to trigger SF and fuel an AGN. Similarly to infalling galaxies experiencing ICM ram pressure (e.g., Gunn et al. 1972), the shock interaction model predicts a disruption of the gaseous disk in galaxies located in the wake of the shock fronts and the presence of tails, knots, or filaments of ionized gas aligned with the merger axis (e.g., Ebeling & Kalita 2019).

What causes the surprising SFR in the “Sausage” cluster galaxies? In this Letter, we put the shock-induced SF model to the test. We present Gemini Gemini Multi-Object Spectrograph-North (GMOS-N) integral field unit (IFU) spectroscopic observations of five, $H\alpha$ -selected, star-forming, active galaxies within the “Sausage” cluster (see Figure 1, Table 1), which unveil the $H\alpha$ and $[N \text{ II}]$ (6585 \AA) gas dynamics, the detailed $H\alpha$ morphologies, and resolved metallicities and provide direct

proof on whether the ionized gas regions in cluster galaxies are disrupted by the passage of the shock waves.

We assume a flat Λ CDM cosmology, with $H_0 = 70.0 \text{ km s}^{-1} \text{ Mpc}^{-1}$, $\Omega_m = 0.3$ and $\Omega_\Lambda = 0.7$. At the redshift of the cluster, $1'' = 3.142 \text{ kpc}$.

2. Targets, Observations, and Data Reduction

2.1. Target Selection

Our targets are drawn from our SFR limited narrow-band survey, which uniformly selects $H\alpha$ emitters in the “Sausage” cluster and the cosmic web around it (Stroe et al. 2015b). For the present study, we focus on five galaxies (see Figures 1, 2 and Table 1), confirmed as cluster members in our follow-up spectroscopic survey (Sobral et al. 2015). For the IFU follow-up, the targets were chosen to be massive ($\gtrsim 2 \times 10^9 M_\odot$), bright, with $H\alpha$ fluxes of $\gtrsim 10^{-15} \text{ erg s}^{-1} \text{ cm}^{-1}$, and *i*-band magnitudes between 17 and 20 mag (AB), and spatially extended over $\gtrsim 5''$ (equivalent to $\gtrsim 16 \text{ kpc}$). The galaxies are located in post-shock regions, traversed by shock waves as recently as 500 Myr. Three galaxies are powered primarily by SF, while two have significant contributions from AGN, while still presenting morphologies consistent with spiral structure. Based on the 1D spectroscopy, two galaxies have evidence for

Table 1

Basic Properties of The Galaxies, Including Coordinates, Redshift, Stellar Mass, $H\alpha$ Flux, i -band AB Magnitude, an Estimate of the Hubble Morphological Classification, and the Classification as SF or AGN from the 1D Spectroscopy (Measurements from Sobral et al. 2015)

Target	R.A. hh: mm: ss.ss	Decl. °: ′: ″	z	M_* ($10^9 M_\odot$)	$F_{H\alpha}^a$ (10^{-15} erg s $^{-1}$ cm $^{-2}$)	i^b (mag)	Morphology	Classification
Sausage 5	22:43:12.90	+53:00:10.08	0.182475	3.9 ± 1.6	1.78	18.94	SBa	SF
Sausage 6	22:42:59.85	+53:02:14.57	0.1836	2.6 ± 1.7	1.88	18.70	SBc	SF
Sausage 7	22:42:57.63	+53:05:14.75	0.18315	33.5 ± 10.6	2.13	17.72	Sb	SF + outflows
Sausage 8	22:43:08.88	+53:05:25.04	0.1843	42.8 ± 13.2	4.06	17.42	SBa	AGN
Sausage 9	22:42:41.07	+52:58:28.67	0.18394	45.1 ± 13.8	5.14	17.35	Sb	AGN + outflows

Notes.^a Errors typically <10%.^b Errors <0.01 mag.

outflows, powered by SF or AGN (Sobral et al. 2015). As such, the sample enables us to test the effect of the cluster merger and the shock waves on the triggering of SF and black hole activity.

2.2. Observations and Data Reduction

We observed five galaxies with GMOS⁶ in the IFU mode (Gemini program GN-2018B-Q-318; PI: A. Stroe). With the two-slit configuration, the observations covered a $5'' \times 7''$ field of view (FoV) centered on the galaxy, and a $5'' \times 3''.5$ sky area, offset by $1'$ from the target. We obtained six exposures of 813 s for each target in queue mode observing, taking advantage of the poorer observing conditions at Maunakea, with gray moon, cloudy weather, and image quality varying between $0''.50$ and $0''.75$ at zenith, as measured on a point source during acquisition. We used the R150 grating in combination with the GG455 filter and a central wavelength of 7300 \AA and 7600 \AA to cover the wavelength gaps. This setup results in a contiguous $5100\text{--}9900 \text{ \AA}$ coverage at $\sim 300 \text{ km s}^{-1}$ resolution.

2.3. Data Reduction

The data were reduced with the Py3D data reduction package for fiber-fed IFU spectrographs initially developed for the CALIFA survey (Husemann et al. 2013). It has already been successfully applied to similar GMOS IFU data beforehand (e.g., Husemann et al. 2016). We perform basic reduction steps on individual exposures that include bias subtraction, cosmic ray cleaning using PyCosmic (Husemann et al. 2012), fiber identification, fiber tracing, stray light subtraction, optimal spectral extraction, wavelength calibration based on CuAr arc lamps, and fiber flat-fielding based on a twilight observation. The standard star Wolf 1346, used as flux calibrator, is calibrated in the same way as the data to determine the sensitivity curve for the given instrumental setup. The individual exposures were flux calibrated before a mean sky background spectrum was constructed from the dedicated offset sky fiber and subsequently subtracted from all fiber spectra in the target FoV. A final data cube is reconstructed by drizzling (Fruchter & Hook 2002) all fibers into a regular grid of squared pixels with a $0''.2$ sampling. With emission lines masked, we collapsed the cube between 7400 and 8150 \AA to obtain a continuum image, which was used to refine the astrometry (within $0''.2$) and precisely align the IFU for each galaxy to its i -band image.

We employ a 2D Gaussian filter with a 1.2 pixel standard deviation to spatially smooth the data. Overall, we find excellent agreement between spectra extracted in $1''.6$ apertures from the IFU observations and our slit and fiber observations from Sobral et al. (2015; see Figure 2). $H\alpha$ and [N II] are detected at high signal-to-noise ratio (S/N) in all the galaxies, while faint continuum emission and $H\beta$, [O III] and [S II] are detected at lower S/N only in some of the galaxies. For the rest of the Letter, we focus solely on the analysis of the $H\alpha$ and [N II] emission lines in line with our main science goals.

3. Analysis

We use the Galaxy Line Emission & Absorption Modelling (GLEAM⁷) Python package (Stroe 2020) to jointly fit the $H\alpha$ and [N II] emission lines and the continuum emission for each spaxel in the smoothed GMOS-N cubes. A window 140 \AA wide around $H\alpha$ and [N II] is modeled with a constant plus two Gaussian models⁸, which are all free parameters in the fit. The redshift measured from the 1D spectroscopy (Sobral et al. 2015) is used as starting solution for the Gaussian center. The positions of $H\alpha$ and [N II] was allowed to independently vary within 9 \AA (or $\pm 350 \text{ km s}^{-1}$) around the wavelength predicted by the systemic redshift. We require a S/N of 3 for emission line detections.

We build flux, velocity, and dispersion maps from the continuum subtracted fluxes and line velocities, as reported from the Gaussian fits (Figure 3) and associated S/N and error maps (Figure 4). The minimum dispersion measurable (120 km s^{-1}) is limited by the instrumental resolution. For SF-dominated galaxies and in regions where both [N II] and $H\alpha$ are detected at $S/N > 3$, we use the [N II]/ $H\alpha$ line ratio to derive spatially resolved metallicity maps (Figure 3). Using the calibration from Pettini & Pagel (2004), we convert the [N II]/ $H\alpha$ ratio to metallicity (oxygen abundance): $12 + \log_{10}(\text{O}/\text{H}) = 8.9 + 0.57 \log_{10}([\text{NII}]/H\alpha)$.

4. Flux, Dynamics and Metallicity Maps

Figure 3 shows a gallery of our five targets, unveiling their $H\alpha$ flux, $H\alpha$ velocity, and dispersion, together with an i -band optical image. We also show a metallicity map for the star-forming galaxies. We robustly detect dynamics of nebular $H\alpha$ and [N II] emission extended over 16 kpc in all five galaxies, with evidence for disturbed morphologies, including tails of

⁶ <http://www.gemini.edu/instrumentation/current-instruments/gmos>

⁷ <https://github.com/multiwavelength/gleam>

⁸ [N II] (6550 \AA) contribution is negligible.

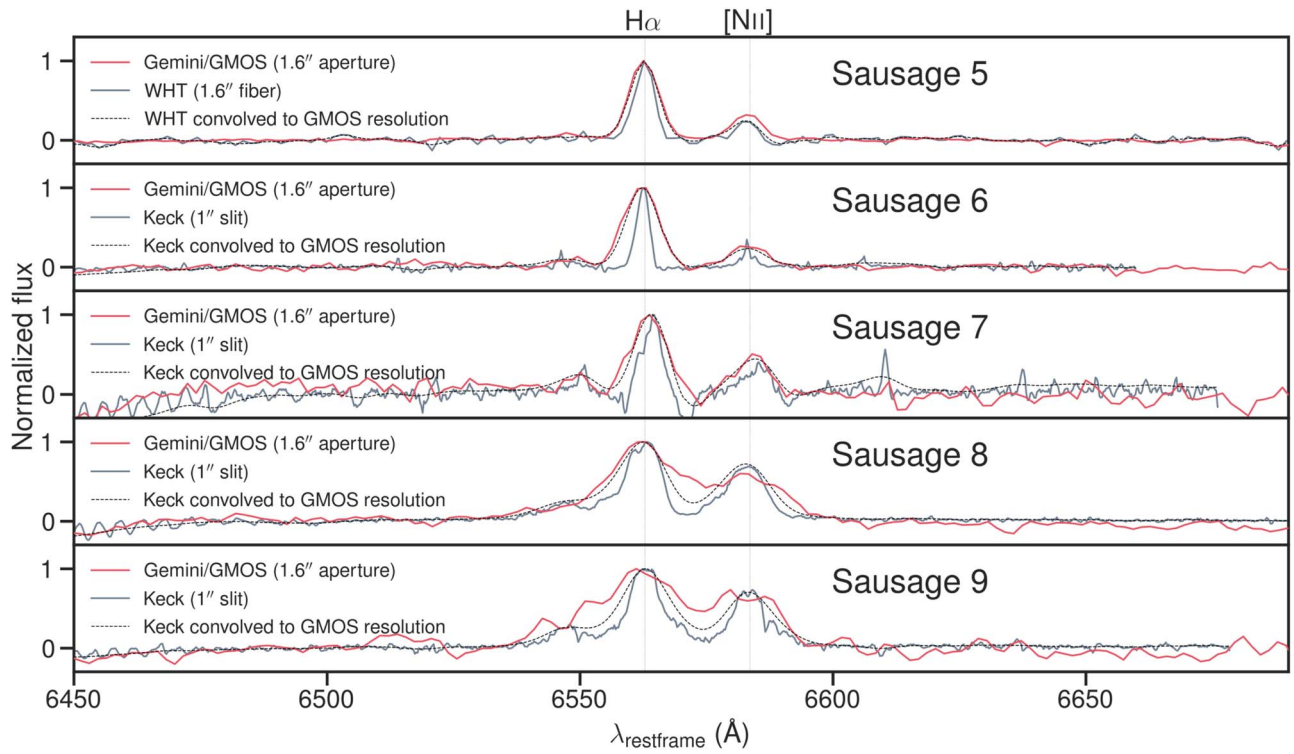


Figure 2. Aperture ($1''.6$) spectra extracted from the Gemini/GMOS IFU observations are in excellent agreement with the 1D spectra from our $1''.6$ fiber and $1''$ slit observations (Sobral et al. 2015). The spectra are continuum subtracted and normalized to the $H\alpha$ peak.

ionized gas offset from the stellar disk. The metallicity maps show diverse distributions.

Sausage 5, 6, 7 are firmly classified as SF spiral galaxies based on line ratios in their 1D spectra (Sobral et al. 2015). Further evidence to support this scenario comes from the IFU data, where the emission is consistent with photoionization throughout the galaxies, considering the small ratios between the [S II] doublet (which in many cases is not detected) and $H\alpha$ (Kewley et al. 2006). All three galaxies have strong $H\alpha$ velocity gradients with comparatively low dispersions, confirming their rotating nature. All three galaxies have bright knots of ionized gas emission with high relative velocities of $\pm 300 \text{ km s}^{-1}$. Generally, the $H\alpha$ flux extensions follow the motion of the disk, but with larger amplitudes in velocity. In Sausage 5, the peak of the $H\alpha$ emission is offset in the north direction by about $0''.2$ ($\sim 0.6 \text{ kpc}$). The ionized nebular gas in Sausage 5 has an asymmetric rotation pattern with higher amplitude in velocity on the approaching side ($\sim -100 \text{ km s}^{-1}$ with $7\text{--}8 \text{ km s}^{-1}$ uncertainty per pixel) and velocities of up to $70 \pm 23 \text{ km s}^{-1}$ at the northern tip, an offset flux peak toward the northwest from the stellar disk. The tails and spurs of ionized gas are detected at S/N $\sim 4\text{--}10$ per pixel across the features. For example, in Sausage 6, the $H\alpha$ emission peak, embedded in a region of metal-poor gas (8.5 ± 0.05 per pixel) is offset $0''.6$ ($\sim 1.9 \text{ kpc}$) northwest from the peak of the stellar emission, followed by a spur of extremely metal-rich gas (9.0 ± 0.05 per pixel) toward the northwest of the galaxy (offset $3''.7$ west and $1''.2$ north from the stellar disk center). In Sausage 7, the ionized gas maps look remarkably different from the stellar distribution. The bright nucleus surrounded by a well-defined spiral structure is not reflected in the complex, clumpy $H\alpha$ gas, whose bow-like distribution is offset north from the stellar disk. The peak of the $H\alpha$ emission is also offset $0''.5$ ($\sim 1.6 \text{ kpc}$) from the peak of the stellar light. The metallicity has a strong 0.2 dex gradient along

the disk of the galaxy, with elevated values on the side closest to the northern cluster-scale shock front.

While the emission-line budget in both Sausage 8 and 9 is dominated by AGN contribution (Sobral et al. 2015), the resolved IFU observations reveal a more complex picture. With the fastest $H\alpha$ rotational velocities but also the largest gas dispersions of the sample (over $\sim 400 \text{ km s}^{-1}$), Sausage 9 is a classical Seyfert 1 type source, with a bright nucleus dominated by AGN emission, broad emission lines, and a pronounced spiral arm pattern powered by SF, recovered in both the i -band and the ionized gas maps. The peak of $H\alpha$ emission is offset south in Sausage 9, by $\sim 0.9 \text{ kpc}$ with respect to the optical nucleus. Sausage 8 shows two tails of $H\alpha$ emission distinct from the general disk rotation pattern: one tail of redshifted gas and a spur of blueshifted $H\alpha$ emission toward the northwest.

5. Discussion

We explore the role of the merging cluster environment in triggering sustained SF in five massive, gas-rich, main-sequence galaxies in the post-shock region within the ‘‘Sausage’’ cluster. Our IFU observations reveal morphological and kinematical disturbances in the nebular gas, generally aligned with the merger axis of the cluster. Our main aim is to disentangle whether the high-significance tails, spurs, and knots are caused by infall and interaction with the ICM, by galaxy-galaxy mergers/interactions or by a cluster-wide process, such as a merger-induced shock.

5.1. Infalling Galaxies?

The majority of isolated and undisturbed galaxies have regular kinematic maps and strong negative gas-phase metallicity gradients (e.g., Poetrodjojo et al. 2018), explained by an inside-out disk formation model, where the central metal-rich

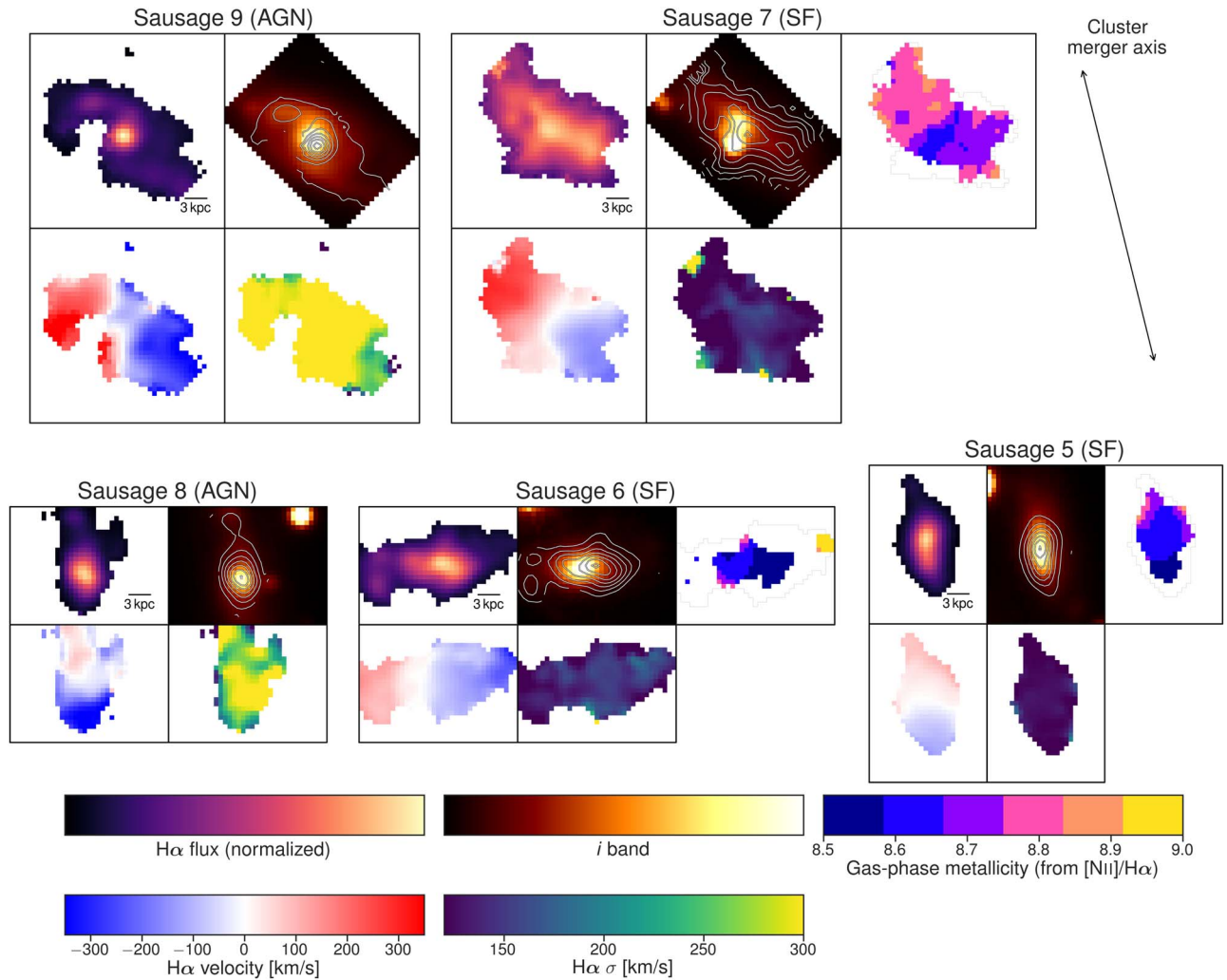


Figure 3. A gallery of “shocked” galaxies in the “Sausage” cluster merger. For each galaxy, clockwise from the top left, we show the $H\alpha$ flux map, i -band Subaru/Suprime-Cam image with $H\alpha$ flux contours, $H\alpha$ dispersion, and velocity map. For SF-dominated galaxies, we also show the metallicity map, with the $H\alpha$ detection border shown in light gray. All galaxies show evidence for morphologies and kinematics disturbed in the north–south direction. The alignment with the merger axis of the cluster suggests a tight connection between the merger event and the triggering of SF. Corresponding S/N and error maps can be found in Figure 4.

(The data used to create this figure are available.)

region has been undergoing sustained SF for longer than the metal-poor gas at the outskirts of the galaxy (e.g., Pilkington et al. 2012). For star-forming cluster galaxies, we might expect a large fraction of disturbed $H\alpha$ kinematics and morphologies due to the interaction with the ICM during their infall and gravitational perturbations (Cortese et al. 2007). However, in their large sample of $H\alpha$ -selected galaxies, Tiley et al. (2020) find a variety of $H\alpha$ morphologies, including regular, centrally peaked distributions with disk-like velocity maps and irregular distributions in both field and cluster environments, as galaxies undergoing significant quenching would not be included in their $H\alpha$ -selected sample.

A particularly interesting class to compare with are jellyfish galaxies: these are galaxies infalling into clusters that exhibit gaseous tails with bright star-forming knots caused by ram pressure. Despite the extreme interaction with the ICM, jellyfish galaxies display strong negative gas-phase metallicities from the center toward the stripped tails, consistent with an inside-out formation in isolation, followed by a outside-in removal of gas upon infall into the cluster (e.g., Bellhouse et al. 2019;

Franchetto et al. 2020). Our galaxies show offset $H\alpha$ -flux peaks, extended tails of nebular emission, and bow-like and asymmetric velocity maps reminiscent of those seen in jellyfish galaxies. However, the tantalizing alignment of these features with the merger axis is broadly incompatible with galaxies infalling into the cluster radially and, unlike jellyfish galaxies, we actually find consistent evidence against radial metallicity gradients.

We can draw comparisons between detailed studies of infalling galaxies in local clusters. For example, Chemin et al. (2006) conducted a detailed kinematic analysis of 30 typical spiral galaxies in the $1.2 \times 10^{15} M_{\odot}$ Virgo cluster, located at a distance of just ~ 16.5 Mpc. The bulk of their sample is located outside the core of the cluster, specifically at relative velocities and radii larger than our sample (see the phase-space diagram in Figure 5). Chemin et al. (2006) found evidence for disturbed $H\alpha$ kinematics, but the offsets between the peak of the stellar light and the $H\alpha$ are of the order of 0.2–0.4 kpc, which is smaller than what we observe in our galaxies (0.6–1.9 kpc). Outside of its core, the Coma cluster ($7 \times 10^{14} M_{\odot}$, located at

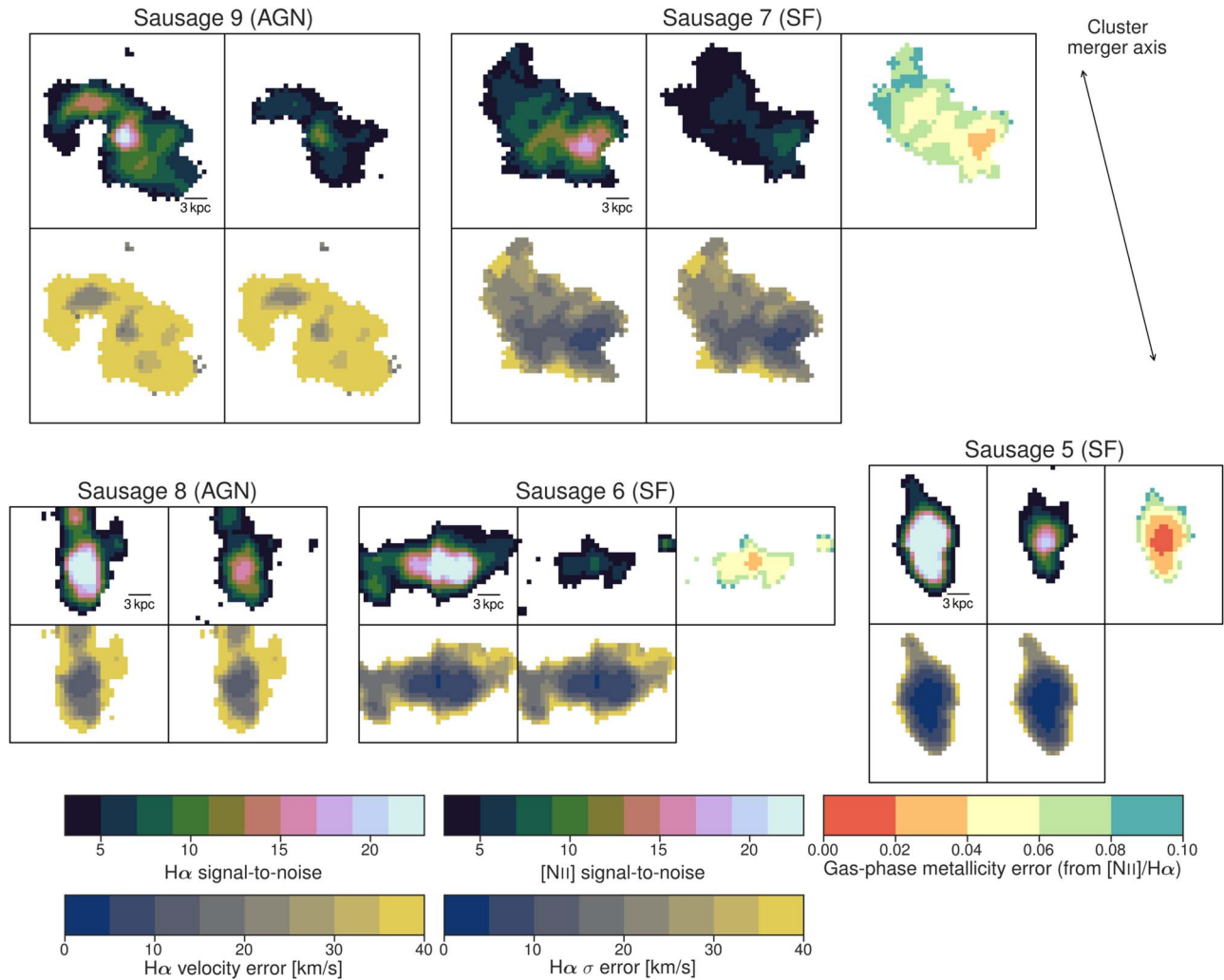


Figure 4. Error maps corresponding to the gallery of galaxies presented in Figure fig:gallery. For each galaxy, clockwise from the top left, we show the $H\alpha$ S/N map, the $[N II]$ S/N map, the $H\alpha$ velocity dispersion uncertainty map, and $H\alpha$ velocity uncertainty map. For star-forming galaxies, we also show the metallicity error map. In the $[N II]$ flux and metallicity maps we show the border of the $H\alpha$ emission in light gray.

~ 100 Mpc) is dominated by disturbed galaxies with tails of $H\alpha$ emission (Gavazzi et al. 2018). Three Coma galaxies are located to the cluster center as close as our galaxies Sausage 6–9 (Figure 5). However, these three galaxies are undergoing extreme ram pressure. With only one galaxy powered by SF and two by AGN, there is little to no $H\alpha$ within the stellar disk and the bulk of $H\alpha$ is found outside the galaxies, streaming out in long tails (Yagi et al. 2010). Observations of both Coma and Virgo indicate that infalling galaxies can present tails of $H\alpha$ emission and perturbed kinematics, but the $H\alpha$ gas is removed from the outside in, while the peak of the emission, close to the nucleus of the galaxies does not get displaced.

Considering that our galaxies are deeply embedded in the hottest parts of the ICM (see Figure 5) and present disturbed morphologies and kinematics throughout and outside the stellar disk, it is improbable that the nebular gas features are caused by ram pressure in infalling galaxies. The orientation of the gas tails imply infall pathways for galaxies 6, 7, 8, and 9, which would cross the densest, hottest parts of the ICM. Under the assumption of infall, the gas reservoirs in these galaxies would be almost completely depleted, as evidenced by detailed analyses of the Coma and Virgo clusters (Chemin et al. 2006; Yagi et al. 2010; Gavazzi et al. 2018).

5.2. Interacting Galaxies?

The kinematic disturbances seen in our sample are reminiscent of those seen in interacting or merging galaxies (e.g., Torres-Flores et al. 2014). Additionally, metallicity gradients can be much shallower in lower-mass galaxies and galaxies that are disturbed, for example by a tidal interaction or a merger with another galaxy that can funnel pristine, metal-poor gas toward the core of the galaxy (see the review by Kewley et al. 2019). The interaction scenario explains some, but not all, of the observations: our galaxies maintain regular kinematics within the bulk of the stellar light and all three star-forming galaxies have metallicity gradients across the stellar disk. Because galaxy–galaxy interactions are most common in low-mass clusters and group-like environments, it is highly unlikely that all five galaxies are undergoing mergers in an extremely massive, $2 \times 10^{15} M_{\odot}$ cluster such as the “Sausage.”

5.3. SF Induced by Cluster Merger?

Fast-traveling, relatively low-Mach number ($M \sim 1-4$) shocks, such as those produced in cluster mergers (Roediger et al. 2014), possibly compounded with the time-dependent tidal fields of merging clusters (e.g., Bekki 1999) are expected

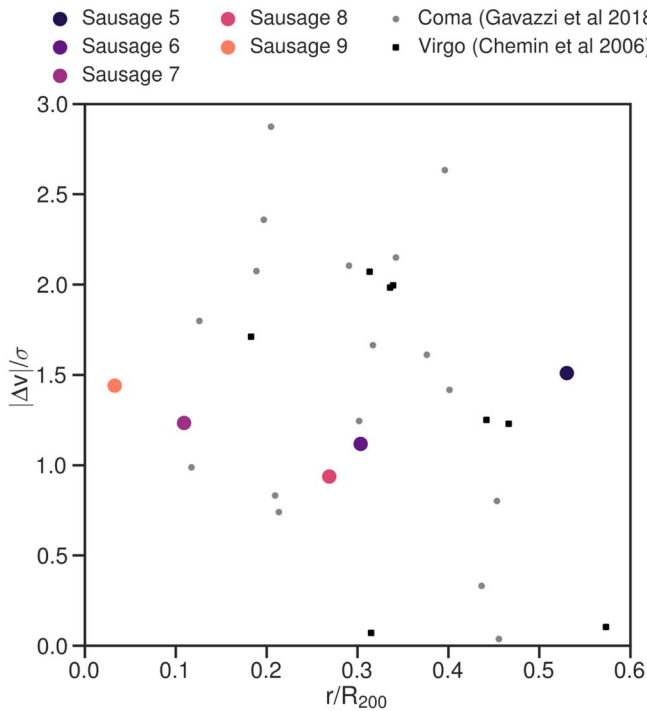


Figure 5. Phase-space diagram for the cores of the Sausage, Virgo, and Coma clusters, highlighting kinematically disturbed $H\alpha$ galaxies. We show our five galaxies with respect to the properties of the closest subcluster (as derived from weak lensing and dynamics in Jee et al. 2015), together with data from Chemin et al. (2006) on the Virgo cluster and Gavazzi et al. (2018) for the Coma cluster. Our galaxies are embedded deep within the ICM. Unlike galaxies at similar cluster-centric radii and relative velocities in Coma and Virgo, which are almost completely devoid of $H\alpha$ within the disk, the Sausage galaxies show $H\alpha$ throughout the stellar disk, with large offsets between the peak of $H\alpha$ and the stellar light.

to result in elevated pressure that compresses the interstellar medium, not only at the outskirts, but also deep within galaxies, and results in galaxy-wide SF sustained on 100–500 Myr timescales. The features we observe in the flux, velocity and metallicity maps of our galaxies can be ascribed to this scenario. Unlike a galaxy–galaxy merger, the shock front would not “destroy” the disk structure of the galaxy, but cause ionized tails broadly aligned with the merger direction and propagation direction of the shock. This is reflected in our nebular gas kinematic maps, which have disk-like kinematics with $H\alpha$ and [N II] tails, spurs, and offsets in the general north–south direction, despite the range of position angles the galaxies span on the sky. The metallicity maps reveal SF trends that are inconsistent with a simple inside-out disk formation scenario. Located only 500 kpc away from the northern shock front, Sausage 7 was traversed by the shock less than 200 Myr ago and is thus expected to show strong evidence for shock interaction. Indeed, the source’s elevated metallicities support a scenario of elevated SF activity throughout the galaxy. The star-forming sources all show metallicity gradients across the galaxy disk that broadly follow the distribution of the disrupted offset nebular gas, suggesting a plausible causal connection between the shock disruption and the triggering of SF. Overall, SF is quenched in clusters with significant populations of galaxies disturbed by ram pressure or tidal fields. By contrast, the Sausage cluster presents ample evidence of a significant enhancement of SF (Stroe et al. 2015a, 2017). If ram pressure or tidal disruption alone cause the features in our velocity,

metallicity and gas maps, similar SF enhancements, should be visible in other clusters. When taking all evidence into account, both presented in the present Letter and in previous analyses, the simplest scenario that explains all the data suggests a likely causal connection between the merger of the cluster and the features observed in our data.

6. Conclusion

We presented the first resolved IFU spectroscopic observations of five $H\alpha$ -selected main-sequence galaxies in the low-redshift ($z \sim 0.2$), massive ($\sim 2 \times 10^{15} M_{\odot}$), “Sausage” merging cluster, which displays a surprising reversal of the typical environmental trends observed in $z < 1$ clusters. The five galaxies have disk-like $H\alpha$ morphologies and kinematics, with evidence of disturbed $H\alpha$ and [N II] tails and spurs aligned with the merger axis of the cluster. Metallicity gradients are consistent with SF triggered throughout the galaxies. These observations possibly present the most direct evidence for SF induced by the merger of massive galaxy clusters and their associated large-scale shock waves, especially when combined with previous results of elevated SF in the “Sausage” cluster.



The pilot observations shown here demonstrate that leaps in our understanding of galaxy cluster physics are achievable with IFUs, even with modest telescope time investments. Future studies of statistically significant samples will disentangle shock, merger, and ram-pressure contributions in triggering SF across a range of local densities and stellar masses.

We thank the referee for their excellent comments that have improved this Letter. We thank Adrian Bittner, Jorjyt Matthee, and Rebecca Nevin for useful discussions. A.S. gratefully acknowledges support of a Clay Fellowship. M.H. acknowledges the Smithsonian Astrophysical Observatory REU program, which is funded in part by the National Science Foundation REU and Department of Defense ASSURE programs under NSF grant no. AST-1852268, and by the Smithsonian Institution. B.H. acknowledges financial support by the DFG grant GE625/17-1 and DLR grant 50OR1911. We thank Matthew Ashby and Jonathan McDowell for comments on an early draft. Based on observations obtained at the international Gemini Observatory, a program of NSF’s NOIRLab, which is managed by the Association of Universities for Research in Astronomy (AURA) under a cooperative agreement with the National Science Foundation, on behalf of the Gemini Observatory partnership: the National Science Foundation (United States), National Research Council (Canada), Agencia Nacional de Investigación y Desarrollo (Chile), Ministerio de Ciencia, Tecnología e Innovación (Argentina), Ministério da Ciência, Tecnologia, Inovações e Comunicações (Brazil), and Korea Astronomy and Space Science Institute (Republic of Korea). Based in part on data collected at Subaru Telescope, which is operated by the National Astronomical Observatory of Japan. The authors wish to recognize and acknowledge the very significant cultural role and reverence that the summit of Maunakea has always had within the indigenous Hawaiian community. We are most fortunate to have the opportunity to conduct observations from this mountain.

Facilities: Gemini:Gillett (GMOS-N), Subaru (Suprime-Cam), CXO (ACIS-I), GMRT.

Software: gleam (Stroe 2020), Astropy (Astropy Collaboration et al. 2013), APLpy (Robitaille & Bressert 2012), DS9 (Joye & Mandel 2003), QFitsView.

ORCID iDs

Andra Stroe  <https://orcid.org/0000-0001-8322-4162>
 Maryam Hussaini  <https://orcid.org/0000-0001-9580-1043>
 David Sobral  <https://orcid.org/0000-0001-8823-4845>
 Grant Tremblay  <https://orcid.org/0000-0002-5445-5401>

References

- Andrade-Santos, F., Jones, C., Forman, W. R., et al. 2017, *ApJ*, **843**, 76
 Astropy Collaboration, Robitaille, T. P., Tollerud, E. J., et al. 2013, *A&A*, **558**, A33
 Bekki, K. 1999, *ApJL*, **510**, L15
 Bellhouse, C., Jaffe, Y. L., McGee, S. L., et al. 2019, *MNRAS*, **485**, 1157
 Cairns, J., Stroe, A., Breuck, C. D., Mroczkowski, T., & Clements, D. 2019, *ApJ*, **882**, 132
 Chemin, L., Balkowski, C., Cayatte, V., et al. 2006, *MNRAS*, **366**, 812
 Cortese, L., Gavazzi, G., Boselli, A., Iglesias-Paramo, J., & Carrasco, L. 2004, *A&A*, **425**, 429
 Cortese, L., Marcellac, D., Richard, J., et al. 2007, *MNRAS*, **376**, 157
 Dressler, A. 1980, *ApJ*, **236**, 351
 Ebeling, H., & Kalita, B. S. 2019, *ApJ*, **882**, 127
 Franchetto, A., Vulcani, B., Poggianti, B. M., et al. 2020, *ApJ*, **895**, 106
 Fruchter, A. S., & Hook, R. N. 2002, *PASP*, **114**, 144
 Gavazzi, G., Consolandi, G., Gutierrez, M. L., Boselli, A., & Yoshida, M. 2018, *A&A*, **618**, A130
 Gunn, J. E., Gott, J., & Richard, I. 1972, *ApJ*, **176**, 1
 Hou, A., Parker, L. C., Wilman, D. J., et al. 2012, *MNRAS*, **421**, 3594
 Husemann, B., Jahnke, K., Sánchez, S. F., et al. 2013, *A&A*, **549**, A87
 Husemann, B., Kamann, S., Sandin, C., et al. 2012, *A&A*, **545**, A137
 Husemann, B., Scharwächter, J., Bennert, V. N., et al. 2016, *A&A*, **594**, A44
 Hwang, H. S., & Lee, M. G. 2009, *MNRAS*, **397**, 2111
 Jaffé, Y. L., Poggianti, B. M., Verheijen, M. A. W., Deshev, B. Z., & van Gorkom, J. H. 2012, *ApJL*, **756**, L28
 Jaffé, Y. L., Verheijen, M. A. W., Haines, C. P., et al. 2016, *MNRAS*, **461**, 1202
 Jee, M. J., Stroe, A., Dawson, W., et al. 2015, *ApJ*, **802**, 46
 Joye, W. A., & Mandel, E. 2003, in ASP Conf. Ser. 295, *Astronomical Data Analysis Software and Systems XII*, ed. H. E. Payne, R. I. Jedrzejewski, & R. N. Hook (San Francisco, CA: ASP), 489
 Kewley, L. J., Groves, B., Kauffmann, G., & Heckman, T. 2006, *MNRAS*, **372**, 961
 Kewley, L. J., Nicholls, D. C., & Sutherland, R. S. 2019, *ARA&A*, **57**, 511
 Lewis, I., Balogh, M., De Propriis, R., et al. 2002, *MNRAS*, **334**, 673
 Mahajan, S., Haines, C. P., & Raychaudhury, S. 2010, *MNRAS*, **404**, 1745
 Mann, A. W., & Ebeling, H. 2012, *MNRAS*, **420**, 2120
 Miller, N. A., & Owen, F. N. 2003, *AJ*, **125**, 2427
 Muldrew, S. I., Hatch, N. A., & Cooke, E. A. 2015, *MNRAS*, **452**, 2528
 Ogrea, G. A., Brüggén, M., van Weeren, R., et al. 2014, *MNRAS*, **440**, 3416
 Pettini, M., & Pagel, B. E. J. 2004, *MNRAS*, **348**, L59
 Pilkington, K., Gibson, B. K., Brook, C. B., et al. 2012, *MNRAS*, **425**, 969
 Poetrodjojo, H., Groves, B., Kewley, L. J., et al. 2018, *MNRAS*, **479**, 5235
 Ricker, P. M., & Sarazin, C. L. 2001, *ApJ*, **561**, 621
 Robitaille, T., & Bressert, E. 2012, APLpy: Astronomical Plotting Library in Python, Astrophysics Source Code Library, ascl:1208.017
 Roediger, E., Brüggén, M., Owers, M. S., Ebeling, H., & Sun, M. 2014, *MNRAS*, **443**, L114
 Rossetti, M., Gastaldello, F., Eckert, D., et al. 2017, *MNRAS*, **468**, 1917
 Sobral, D., Stroe, A., Dawson, W. A., et al. 2015, *MNRAS*, **450**, 630
 Solanes, J. M., Manrique, A., García-Gómez, C., et al. 2001, *ApJ*, **548**, 97
 Stroe, A. 2020, GLEAM: Galaxy Line Emission Absorption Modelling, v1.0, Zenodo, doi:10.5281/zenodo.3974969
 Stroe, A., Harwood, J. J., Hardcastle, M. J., & Röttgering, H. J. A. 2014a, *MNRAS*, **445**, 1213
 Stroe, A., Oosterloo, T., Röttgering, H. J. A., et al. 2015a, *MNRAS*, **452**, 2731
 Stroe, A., Sobral, D., Dawson, W., et al. 2015b, *MNRAS*, **450**, 646
 Stroe, A., Sobral, D., Paulino-Afonso, A., et al. 2017, *MNRAS*, **465**, 2916
 Stroe, A., Sobral, D., Röttgering, H. J. A., & van Weeren, R. J. 2014b, *MNRAS*, **438**, 1377
 Stroe, A., van Weeren, R. J., Intema, H. T., et al. 2013, *A&A*, **555**, A110
 Tanaka, M., Goto, T., Okamura, S., Shimasaku, K., & Brinkmann, J. 2004, *AJ*, **128**, 2677
 Tiley, A. L., Vaughan, S. P., Stott, J. P., et al. 2020, *MNRAS*, **496**, 649
 Torres-Flores, S., Amram, P., Mendes de Oliveira, C., et al. 2014, *MNRAS*, **442**, 2188
 van Weeren, R. J., Brüggén, M., Röttgering, H. J. A., & Hoefl, M. 2011, *MNRAS*, **418**, 230
 Yagi, M., Yoshida, M., Komiyama, Y., et al. 2010, *AJ*, **140**, 1814
 Yoon, Y., & Im, M. 2020, *ApJ*, **893**, 117
 Yoon, Y., Im, M., Lee, G.-H., Lee, S.-K., & Lim, G. 2019, *NatAs*, **3**, 844